

Improved Measurements of Color-Suppressed Decays

$\bar{B}^0 \rightarrow D^0\pi^0, D^0\eta, D^0\omega, D^{*0}\pi^0, D^{*0}\eta$ and $D^{*0}\omega$

S. Blyth,²³ K. Abe,⁷ K. Abe,⁴³ I. Adachi,⁷ H. Aihara,⁴⁵ D. Anipko,¹ V. Aulchenko,¹ T. Aushev,¹² A. M. Bakich,⁴⁰ V. Balagura,¹² E. Barberio,²⁰ A. Bay,¹⁷ I. Bedny,¹ K. Belous,¹¹ U. Bitenc,¹³ I. Bizjak,¹³ A. Bozek,²⁶ M. Bračko,^{7,19,13} J. Brodzicka,²⁶ T. E. Browder,⁶ M.-C. Chang,⁴⁴ Y. Chao,²⁵ A. Chen,²³ K.-F. Chen,²⁵ W. T. Chen,²³ B. G. Cheon,³ R. Chistov,¹² Y. Choi,³⁹ Y. K. Choi,³⁹ A. Chuvikov,³⁴ S. Cole,⁴⁰ J. Dalseno,²⁰ M. Dash,⁴⁹ A. Drutskoy,⁴ S. Eidelman,¹ S. Fratina,¹³ N. Gabyshev,¹ A. Garmash,³⁴ T. Gershon,⁷ A. Go,²³ G. Gokhroo,⁴¹ B. Golob,^{18,13} A. Gorišek,¹³ H. Ha,¹⁵ J. Haba,⁷ T. Hara,³¹ K. Hayasaka,²¹ H. Hayashii,²² M. Hazumi,⁷ D. Heffernan,³¹ T. Hokuue,²¹ Y. Hoshi,⁴³ S. Hou,²³ W.-S. Hou,²⁵ Y. B. Hsiung,²⁵ T. Iijima,²¹ A. Imoto,²² K. Inami,²¹ A. Ishikawa,⁴⁵ R. Itoh,⁷ M. Iwasaki,⁴⁵ Y. Iwasaki,⁷ J. H. Kang,⁵⁰ N. Katayama,⁷ H. Kawai,² T. Kawasaki,²⁸ H. R. Khan,⁴⁶ H. Kichimi,⁷ H. J. Kim,¹⁶ H. O. Kim,³⁹ Y. J. Kim,⁵ S. Korpar,^{19,13} P. Križan,^{18,13} P. Krokovny,⁷ R. Kumar,³² C. C. Kuo,²³ A. Kuzmin,¹ Y.-J. Kwon,⁵⁰ G. Leder,¹⁰ J. Lee,³⁸ S.-W. Lin,²⁵ D. Liventsev,¹² F. Mandl,¹⁰ T. Matsumoto,⁴⁷ A. Matyja,²⁶ S. McOnie,⁴⁰ W. Mitaroff,¹⁰ K. Miyabayashi,²² H. Miyake,³¹ H. Miyata,²⁸ Y. Miyazaki,²¹ R. Mizuk,¹² G. R. Moloney,²⁰ T. Nagamine,⁴⁴ E. Nakano,³⁰ M. Nakao,⁷ S. Nishida,⁷ O. Nitoh,⁴⁸ S. Ogawa,⁴² T. Ohshima,²¹ T. Okabe,²¹ S. Okuno,¹⁴ S. L. Olsen,⁶ Y. Onuki,²⁸ W. Ostrowicz,²⁶ H. Ozaki,⁷ P. Pakhlov,¹² G. Pakhlova,¹² H. Palka,²⁶ H. Park,¹⁶ K. S. Park,³⁹ R. Pestotnik,¹³ L. E. Piilonen,⁴⁹ Y. Sakai,⁷ T. Schietinger,¹⁷ O. Schneider,¹⁷ J. Schümann,²⁴ C. Schwanda,¹⁰ A. J. Schwartz,⁴ R. Seidl,^{8,35} M. Shapkin,¹¹ H. Shibuya,⁴² B. Shwartz,¹ V. Sidorov,¹ J. B. Singh,³² A. Somov,⁴ N. Soni,³² S. Stanić,²⁹ M. Starić,¹³ H. Stoeck,⁴⁰ T. Sumiyoshi,⁴⁷ S. Suzuki,³⁶ F. Takasaki,⁷ N. Tamura,²⁸ M. Tanaka,⁷ G. N. Taylor,²⁰ Y. Teramoto,³⁰ I. Tikhomirov,¹² X. C. Tian,³³ K. Trabelsi,⁶ T. Tsuboyama,⁷ T. Tsukamoto,⁷ S. Uehara,⁷ T. Uglov,¹² K. Ueno,²⁵ S. Uno,⁷ Y. Usov,¹ G. Varner,⁶ K. E. Varvell,⁴⁰ S. Villa,¹⁷ C. C. Wang,²⁵ C. H. Wang,²⁴ M.-Z. Wang,²⁵ Y. Watanabe,⁴⁶ E. Won,¹⁵ C.-H. Wu,²⁵ Q. L. Xie,⁹ A. Yamaguchi,⁴⁴ Y. Yamashita,²⁷ M. Yamauchi,⁷ L. M. Zhang,³⁷ and Z. P. Zhang³⁷

(The Belle Collaboration)

¹Budker Institute of Nuclear Physics, Novosibirsk

²Chiba University, Chiba

³Chonnam National University, Kwangju

⁴University of Cincinnati, Cincinnati, Ohio 45221

⁵The Graduate University for Advanced Studies, Hayama, Japan

⁶University of Hawaii, Honolulu, Hawaii 96822

⁷High Energy Accelerator Research Organization (KEK), Tsukuba

⁸University of Illinois at Urbana-Champaign, Urbana, Illinois 61801

⁹Institute of High Energy Physics, Chinese Academy of Sciences, Beijing

¹⁰Institute of High Energy Physics, Vienna

¹¹Institute of High Energy Physics, Protvino

¹²Institute for Theoretical and Experimental Physics, Moscow

¹³J. Stefan Institute, Ljubljana

¹⁴Kanagawa University, Yokohama

¹⁵Korea University, Seoul

¹⁶Kyungpook National University, Taegu

¹⁷Swiss Federal Institute of Technology of Lausanne, EPFL, Lausanne

¹⁸University of Ljubljana, Ljubljana

¹⁹University of Maribor, Maribor

²⁰University of Melbourne, Victoria

²¹Nagoya University, Nagoya

²²Nara Women's University, Nara

²³National Central University, Chung-li

²⁴National United University, Miao Li

²⁵Department of Physics, National Taiwan University, Taipei

²⁶H. Niewodniczanski Institute of Nuclear Physics, Krakow

²⁷Nippon Dental University, Niigata

²⁸Niigata University, Niigata

²⁹University of Nova Gorica, Nova Gorica

³⁰*Osaka City University, Osaka*
³¹*Osaka University, Osaka*
³²*Panjab University, Chandigarh*
³³*Peking University, Beijing*
³⁴*Princeton University, Princeton, New Jersey 08544*
³⁵*RIKEN BNL Research Center, Upton, New York 11973*
³⁶*Saga University, Saga*
³⁷*University of Science and Technology of China, Hefei*
³⁸*Seoul National University, Seoul*
³⁹*Sungkyunkwan University, Suwon*
⁴⁰*University of Sydney, Sydney NSW*
⁴¹*Tata Institute of Fundamental Research, Bombay*
⁴²*Toho University, Funabashi*
⁴³*Tohoku Gakuin University, Tagajo*
⁴⁴*Tohoku University, Sendai*
⁴⁵*Department of Physics, University of Tokyo, Tokyo*
⁴⁶*Tokyo Institute of Technology, Tokyo*
⁴⁷*Tokyo Metropolitan University, Tokyo*
⁴⁸*Tokyo University of Agriculture and Technology, Tokyo*
⁴⁹*Virginia Polytechnic Institute and State University, Blacksburg, Virginia 24061*
⁵⁰*Yonsei University, Seoul*

We present improved measurements of the branching fractions of the color-suppressed decays $\bar{B}^0 \rightarrow D^{(*)0} h^0$, where h^0 represents a light neutral meson π^0 , η or ω . The measurements are based on a data sample of 140 fb^{-1} collected at the $\Upsilon(4S)$ resonance with the Belle detector at the KEKB energy-asymmetric e^+e^- collider, corresponding to seven times the luminosity of the previous Belle measurements. All the measured branching fractions fall in the range $1.4\text{--}2.4 \times 10^{-4}$, which is significantly higher than theoretical predictions based on naive factorization.

PACS numbers: 13.25.Hw, 14.40.Nd

I. INTRODUCTION

The weak decays $\bar{B}^0 \rightarrow D^{(*)0} h^0$ [1], where h^0 represents a light neutral meson, are expected to proceed predominantly through internal spectator diagrams, as illustrated in Fig. 1a. The color matching requirement between the quarks from the virtual W^- and the other quark pair results in these decays being “color-suppressed” relative to decays such as $\bar{B}^0 \rightarrow D^{(*)+} h^-$, which proceed through external spectator diagrams as shown in Fig. 1b.

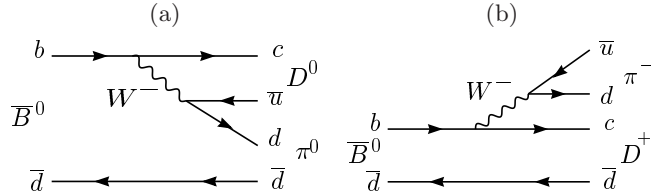


FIG. 1: Tree level internal (a) and external (b) spectator diagrams for $\bar{B} \rightarrow D\pi$ decays.

Previous measurements of \bar{B}^0 decays into $D^0 \rho^0$ [2] and into $D^{(*)0} \pi^0$, $D^0 \eta$ and $D^0 \omega$ [3], by the Belle collaboration, and of \bar{B}^0 into $D^{(*)0} \pi^0$ by the CLEO collaboration [4], and into $D^{(*)0} \pi^0$, $D^{(*)0} \eta$ and $D^{(*)0} \omega$ by the BaBar collaboration [5] all indicate color-suppressed branching fractions in the approximate range $(2\text{--}4) \times 10^{-4}$. Further color-suppressed branching fraction measurements of \bar{B}^0 decays into $D^{(*)0} \eta'$ by the Belle collaboration [6] yield results of approximately $(1.1\text{--}1.2) \times 10^{-4}$. Most of these measurements are substantially in excess of theoretical expectations from “naive” factorization models [7–13], which fall in the range $(0.3\text{--}1.0) \times 10^{-4}$.

Several approaches to achieving a better theoretical description [9, 10, 14, 15] have been developed. They extend upon the factorization approach with consideration of final state interactions and consequent simultaneous treatment of isospin amplitudes of color-suppressed and color-allowed decays. The possibility that similar effects could have dramatic implications on direct CP violation asymmetries in charmless decays, together with some degree of discrepancy

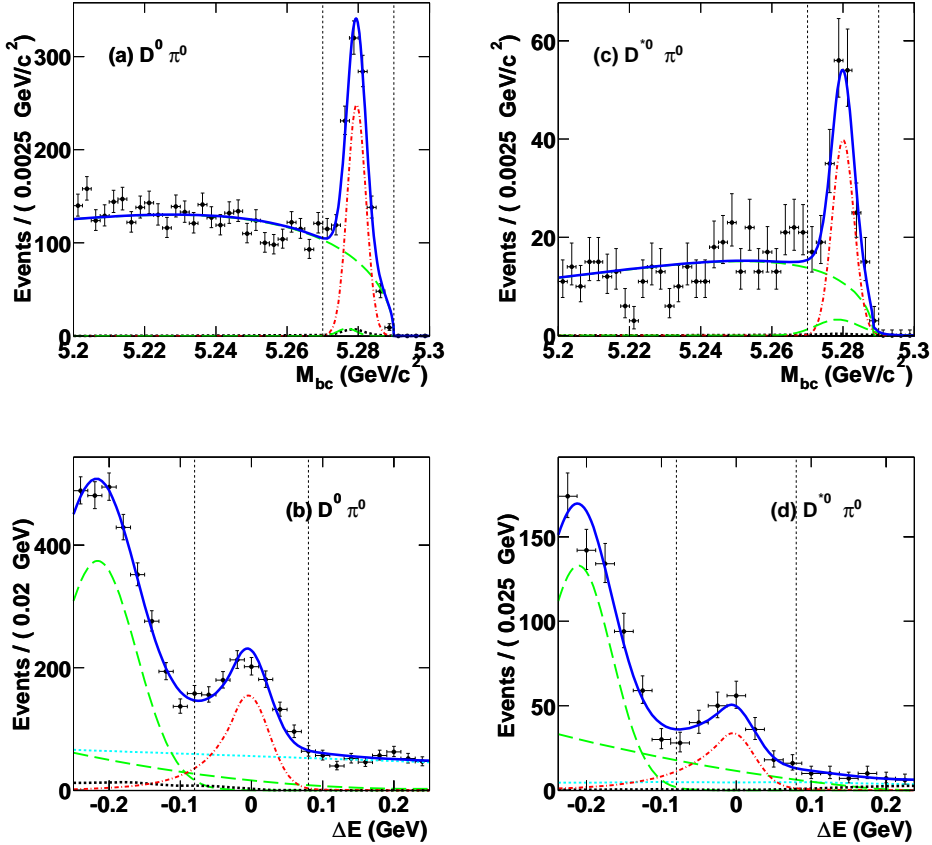


FIG. 2: Distributions of M_{bc} and ΔE for the decay modes $\bar{B}^0 \rightarrow D^0\pi^0$ (a,b) and $\bar{B}^0 \rightarrow D^{*0}\pi^0$ (c,d), with the three D^0 subdecay modes combined. The points represent the data, the solid lines show the result of the fit and the dash-dotted lines (peaking at $\Delta E \approx 0$ GeV and $M_{bc} \approx 5.28$ GeV/c^2) represent the signal contributions. The vertical dotted lines represent the signal region. For the M_{bc} distributions the upper long dashed line shows the continuum-like background contribution, with peaking background contribution represented by the lower long dashed line and cross-feed contribution represented by the bold dotted line. For the ΔE distributions, (b,d) the two long dashed curves show the B background components (dominated by the color allowed $B^- \rightarrow D^{(*)0}\rho^-$ modes) and the dotted line represents the continuum contribution and the bold dotted curve represents the cross-feed contribution.

between the prior Belle [3] and BaBar [5] measurements provide strong motivation for more precise measurements of the color-suppressed decays.

In this paper we report improved branching fraction measurements of \bar{B}^0 decays into $D^0\pi^0$, $D^0\eta$, $D^0\omega$, $D^{*0}\pi^0$, $D^{*0}\eta$ and $D^{*0}\omega$. The measurements are based on a 140 fb^{-1} data sample, which contains 152 million $B\bar{B}$ pairs, collected with the Belle detector at the KEKB asymmetric-energy e^+e^- (3.5 on 8 GeV) collider [16] operating at the $\Upsilon(4S)$ resonance. This corresponds to seven times the luminosity of the previous Belle measurements [3] and almost twice that of the BaBar measurements [5]. Recent measurements of the same processes by the Belle Collaboration [17] have been used to extract the angle ϕ_1 of the CKM Unitarity Triangle using a time-dependent Dalitz analysis of $D \rightarrow K_s^0\pi^+\pi^-$, allowing resolution of the sign ambiguities inherent in other determinations.

The Belle detector is a large-solid-angle magnetic spectrometer that consists of a three-layer silicon vertex detector (SVD), a 50-layer central drift chamber (CDC), an array of aerogel threshold Čerenkov counters (ACC), a barrel-like arrangement of time-of-flight scintillation counters (TOF), and an electromagnetic calorimeter comprised of CsI(Tl) crystals (ECL) located inside a superconducting solenoid coil that provides a 1.5 T magnetic field. An iron flux-return located outside of the coil is instrumented to detect K_L^0 mesons and to identify muons (KLM). The detector is described in detail elsewhere [18].

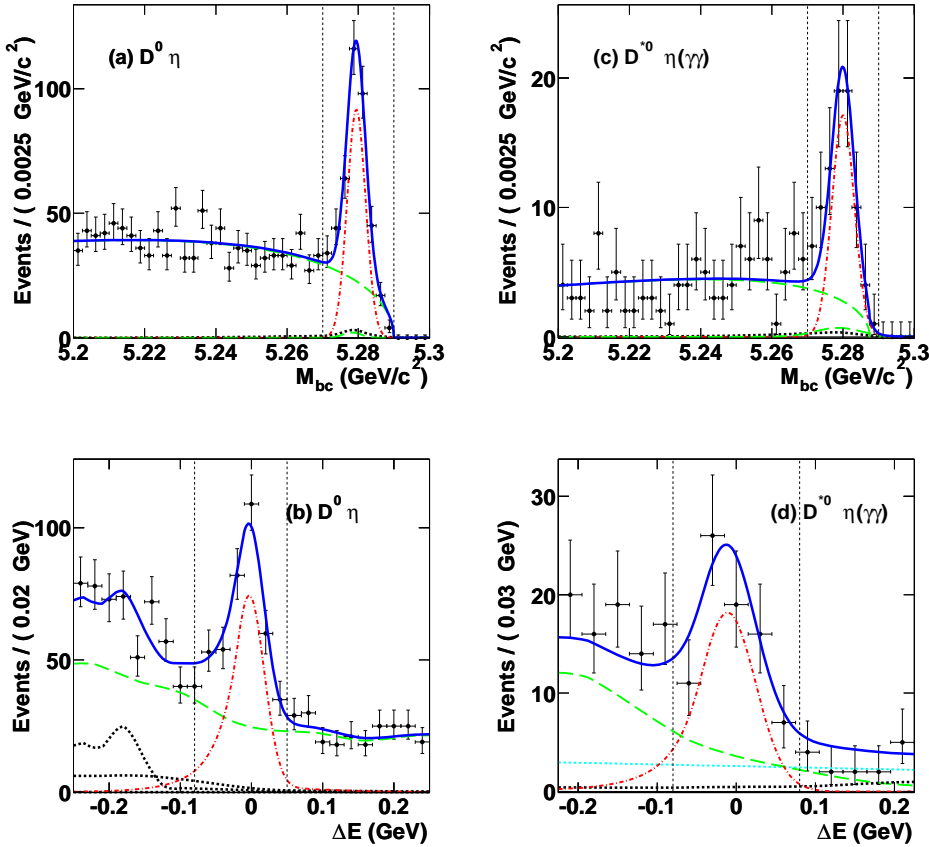


FIG. 3: Distributions of M_{bc} and ΔE for the decay modes $\bar{B}^0 \rightarrow D^0 \eta$ (a,b) and $\bar{B}^0 \rightarrow D^{*0} \eta$ (c,d), with the three D^0 subdecay modes combined. For the ΔE distributions, (b) the long dashed curve represents the sum of B background and continuum contributions; (d) the long dashed curve represents the B background contribution with the dotted line representing the continuum contribution; in both (b,d) the bold dotted curves represent the cross-feed contributions. In (b) two bold dotted curves are visible, corresponding to cross-feed arising from $D^{*0} h^0$ final states; the broader distribution is the component with final states where $D^{*0} \rightarrow D^0 \gamma$ and the other corresponds to final states where $D^{*0} \rightarrow D^0 \pi^0$. Other conventions follow those described in the caption of Figure 2.

II. EVENT SELECTION

Color-suppressed \bar{B}^0 meson decays are reconstructed from candidate D^0 or D^{*0} mesons that are combined with light neutral meson candidates h^0 . The D^0 mesons are reconstructed in the final states $K^- \pi^+$, $K^- \pi^+ \pi^0$, and $K^- \pi^+ \pi^+ \pi^-$, while the light neutral mesons h^0 are reconstructed in the decay modes $\pi^0 \rightarrow \gamma\gamma$, $\eta \rightarrow \gamma\gamma$, $\eta \rightarrow \pi^+ \pi^- \pi^0$ and $\omega \rightarrow \pi^+ \pi^- \pi^0$. The D^{*0} mesons are reconstructed in the $D^{*0} \rightarrow D^0 \pi^0$ decay mode. The decay mode $\bar{B}^0 \rightarrow D^{*0} \eta$ where $\eta \rightarrow \pi^+ \pi^- \pi^0$ is not reconstructed.

Vertex and mass constrained fits are performed for decays with charged products such as the three D^0 decay modes and $\eta \rightarrow \pi^+ \pi^- \pi^0$; mass constrained fits are performed for the $\pi^0 \rightarrow \gamma\gamma$ and $\eta \rightarrow \gamma\gamma$ candidates; and vertex constrained fits are performed for $\omega \rightarrow \pi^+ \pi^- \pi^0$ candidates. These kinematic fits result in reduced uncertainties on the energy and momenta of the candidate mesons.

Charged tracks are required to have impact parameters within ± 5 cm of the interaction point along the beam axis and within 1 cm in the transverse plane. Each track is identified as a kaon or pion according to a likelihood ratio derived from the responses of the TOF and ACC systems and energy loss measurements from the CDC. The likelihood ratio is required to exceed 0.6 for kaon candidates; within the momentum range of interest, this requirement is 88% efficient for kaons and has a misidentification rate for pions of 8.5%.

The photon pairs that constitute π^0 candidates are required to have energies greater than 50 MeV and an invariant

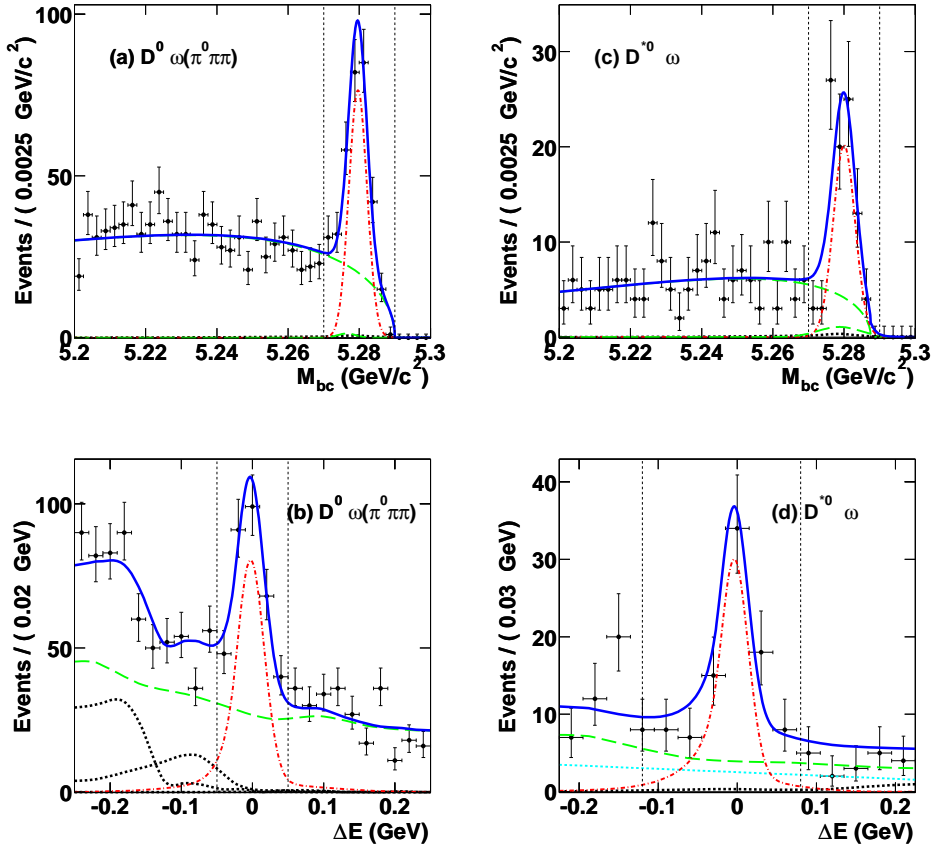


FIG. 4: Distributions of M_{bc} and ΔE for the decay modes $\bar{B}^0 \rightarrow D^0\omega$ (a,b) and $\bar{B}^0 \rightarrow D^{*0}\omega$ (c,d) , with the three D^0 subdecay modes combined. The conventions follow those of Figure 3.

mass within mass windows around the nominal π^0 mass ranging between $\pm 2\sigma$ to $\pm 3\sigma$ depending on the π^0 momentum. The π^0 mass resolution (σ) is momentum dependent, with values in the range $\sigma = 5.4\text{--}9.0 \text{ MeV}/c^2$ over the momentum range of π^0 produced in the $D^{(*)0}\pi^0$ decays considered.

Candidate η mesons that decay to $\gamma\gamma$ are required to have photon energies E_γ greater than 100 MeV. In addition, the energy asymmetry $\frac{|E_{\gamma_1} - E_{\gamma_2}|}{E_{\gamma_1} + E_{\gamma_2}}$, is required to be less than 0.9. The η candidates are required to have invariant masses within a 2.5σ mass window of the nominal mass, where $\sigma = 10.6 \text{ MeV}/c^2$ for the $\eta \rightarrow \gamma\gamma$ mode and $3.4 \text{ MeV}/c^2$ for the $\eta \rightarrow \pi^+\pi^-\pi^0$ mode. If either of the photons that constitute the $\eta \rightarrow \gamma\gamma$ candidate are found to contribute to any $\pi^0 \rightarrow \gamma\gamma$ candidate, the η decay is excluded. The π^0 decay products of the $\eta \rightarrow \pi^+\pi^-\pi^0$ and $\omega \rightarrow \pi^+\pi^-\pi^0$ candidates are required to have center of mass frame (CM) momentum greater than 200 and 500 MeV/c , respectively. The ω candidates are required to have invariant masses within $\pm 3\Gamma$ of the nominal mass value, where Γ is the natural width of the ω meson ($\Gamma = 8.49 \pm 0.08 \text{ MeV}/c^2$ [23]).

Invariant masses of the D^0 candidates are required to be within $\pm 2\sigma$ of the nominal mass, where σ is 8, 12 and 5 MeV/c^2 for the $K^-\pi^+$, $K^-\pi^+\pi^0$, and $K^-\pi^+\pi^+\pi^-$ modes, respectively. The CM momentum of the π^0 in the $K^-\pi^+\pi^0$ mode is required to be greater than 400 MeV/c .

The D^{*0} meson candidates are obtained by combining candidate D^0 and low momentum π^0 mesons, where the soft π^0 momentum in the laboratory frame is required to be less than 0.6 GeV/c and the invariant mass difference $|M(D^{*0}) - M(D^0)|$ is required to be within 2 MeV/c^2 of the nominal value.

III. B RECONSTRUCTION

The \bar{B}^0 candidates are reconstructed from combinations of D^0 or D^{*0} and h^0 using the improved energy and momenta resulting from the vertex and mass constrained fits.

Two kinematic variables are used to distinguish signal candidates from backgrounds: the beam-energy constrained mass $M_{bc} = \sqrt{(E_{beam}^*)^2 - |\sum \vec{p}_i^*|^2}$ and the energy difference $\Delta E = \sum E_i^* - E_{beam}^*$, where E_{beam}^* is the CM energy, and E_i^* , \vec{p}_i^* are the CM energy and momenta, respectively, which are summed over the D^0 or D^{*0} and h^0 meson decay candidates.

The resolution of M_{bc} is approximately $3 \text{ MeV}/c^2$ for all modes, dominated by the beam energy spread, whereas the ΔE resolution varies substantially among modes, depending particularly on the number of π^0 's in the final state. Candidates within the region $|\Delta E| < 0.25 \text{ GeV}$ and $5.2 \text{ GeV}/c^2 < M_{bc} < 5.3 \text{ GeV}/c^2$ are selected for further consideration. Where more than one candidate or reconstruction hypothesis occurs in a single event, a consistency measure is used to pick the best candidate and reconstruction hypothesis. The consistency measure is constructed from the sum of the χ^2 per degree of freedom for the relevant kinematic fits (to D^0 or D^{*0} and h^0). For hypotheses including D^{*0} , an additional term reflecting the deviation of the invariant mass difference $|M(D^{*0}) - M(D^0)|$ from the nominal value is included in the consistency measure. The fraction of events with multiple candidates with the same reconstruction hypothesis in the signal regions defined below is estimated from signal Monte Carlo samples to be less than three percent for all reconstructed modes.

Signal region definitions in M_{bc} and ΔE are chosen based on their resolutions. A common M_{bc} signal region of $5.27 \text{ GeV}/c^2 < M_{bc} < 5.29 \text{ GeV}/c^2$ is used for all final states. The signal regions in ΔE are mode dependent, with $|\Delta E| < 0.08 \text{ GeV}$ for $D^0\pi^0$, $D^0\eta(\gamma\gamma)$, $D^{*0}\pi^0$ and $D^{*0}\eta$ modes ; $-0.08 \text{ GeV} < \Delta E < 0.05 \text{ GeV}$ for $D^0\eta(\pi^0\pi\pi)$; $-0.12 \text{ GeV} < \Delta E < 0.08 \text{ GeV}$ for $D^{*0}\omega$; and $|\Delta E| < 0.05 \text{ GeV}$ for $D^0\omega$.

The event yields and efficiencies presented in the following sections correspond to these signal regions. Figs. 2, 3 and 4 show the M_{bc} and ΔE distributions after application of all selection requirements and with the ΔE signal requirement applied for the M_{bc} distributions (a,c) and the signal requirement $5.27 \text{ GeV}/c^2 < M_{bc} < 5.29 \text{ GeV}/c^2$ applied for the ΔE distributions (b,d). This selection includes continuum suppression requirements as described in the next section. The signal regions are indicated by vertical dashed lines on the figures.

TABLE I: Measured signal region yields and MC estimates of signal region contributions for $\bar{B}^0 \rightarrow D^{(*)0}h^0$ for the combined D^0 subdecay modes. The number of signal events (N_{sig}) obtained from the ΔE fit are listed together with their statistical uncertainties. For the modes $D^{(*)0}\pi^0$ estimates of the background contributions from $D^{(*)0}\rho$ ($N_{D\rho}$) other B backgrounds (N_{bbk}), continuum ($N_{q\bar{q}}$) and cross-feeds (N_{xrs}) are listed. Combined background estimates (N_{bkg}) together with cross-feed contributions (N_{xrs}) are provided for the other D^0h^0 modes. For the other $D^{*0}h^0$ modes, background contributions are shown for B backgrounds (N_{bbk}), continuum ($N_{q\bar{q}}$) and cross-feeds (N_{xrs}).

Mode	N_{sig}	N_{bbk}	N_{bkg}	N_{xrs}	$N_{q\bar{q}}$	$N_{D\rho}$
$D^0\pi^0$	620.5 ± 39.1	26.8 ± 2.1	-	25.9 ± 6.5	448.7 ± 28.0	93.5 ± 8.0
$D^0\eta\gamma\gamma$	160.7 ± 18.3	-	131.8 ± 14.6	6.9 ± 1.7	-	-
$D^0\eta_{\pi^0\pi\pi}^{*0}$	64.7 ± 11.2	-	51.2 ± 8.2	2.4 ± 0.6	-	-
$D^0\eta_{\gamma\gamma+\pi^0\pi\pi}^{*0}$	225.6 ± 21.5	-	174.6 ± 16.0	16.8 ± 4.2	-	-
$D^0\omega$	201.5 ± 20.1	-	135.8 ± 12.9	12.8 ± 3.2	-	-
$D^{*0}\pi^0$	115.2 ± 14.9	22.1 ± 2.9	-	2.0 ± 0.3	29.9 ± 3.9	40.5 ± 5.3
$D^{*0}\eta\gamma\gamma$	49.8 ± 10.0	19.7 ± 3.9	-	2.2 ± 0.4	8.5 ± 1.7	-
$D^{*0}\omega$	53.3 ± 9.2	26.4 ± 4.5	-	1.8 ± 0.3	19.5 ± 3.4	-

[†] The combined η results are from a simultaneous fit to the individual η samples, rather than summation of the individual yields.

IV. CONTINUUM SUPPRESSION

At energies close to the $\Upsilon(4S)$ resonance the production cross section of $e^+e^- \rightarrow q\bar{q}$ ($q = u, d, s, c$) is approximately three times that of $B\bar{B}$ production, making continuum background suppression essential in all modes. The jet-like nature of the continuum events allows event shape variables to discriminate between them and the more-spherical $B\bar{B}$ events.

Seven event-shape variables are combined into a single Fisher discriminant [19]. These variables include the angle between the thrust axis of the B candidate and the thrust axis of the rest of the event ($\cos\theta_T$), the sphericity variable, and five modified Fox-Wolfram moments. The technique and details of the variables used are provided in [19].

Monte Carlo event samples of continuum $q\bar{q}$ events and signal events for each of the final states considered are used to construct probability density functions (PDFs) for the Fisher discriminant [19] and $\cos\theta_B$, where θ_B is the angle between the B flight direction and the beam direction in the CM frame and additional angular variables in some modes, as indicated below. The products of the PDFs for these variables give signal and continuum likelihoods \mathcal{L}_s and $\mathcal{L}_{q\bar{q}}$ for each candidate, allowing a selection to be applied to the likelihood ratio $\mathcal{L} = \mathcal{L}_s/(\mathcal{L}_s + \mathcal{L}_{q\bar{q}})$.

For the decays $\bar{B}^0 \rightarrow D^{*0}\pi^0$ and $D^{*0}\eta$, the vector-pseudoscalar nature of the decay products results in the longitudinal polarization of the D^{*0} . The discrimination benefits from this polarization by incorporating PDFs for the D^{*0} helicity angle in the likelihood ratio. The D^{*0} helicity angle is defined as the angle between the direction of the D^0 and the opposite of the B^0 direction in the D^{*0} rest frame. The vector-vector nature of the decay products in the decay $\bar{B}^0 \rightarrow D^{*0}\omega$ prevents the D^{*0} helicity angle from being a useful discriminant in this mode, as the polarization of the decay products is not known. However, the $\omega \rightarrow \pi^0\pi^+\pi^-$ “splay” angle, defined as the angle between the directions of the π^0 and either the π^+ or π^- in the $\pi^+\pi^-$ rest frame, is found to provide useful discrimination and is incorporated into the likelihood ratio. The method used to account for uncertainties arising from the unknown polarization is described in Section VIII.

Monte Carlo studies of the signal significance $N_s/\sqrt{N_s + N_b}$, where N_s and N_b are Monte Carlo signal and background yields (using signal branching fractions from previous measurements), as a function of a cut on the likelihood ratio \mathcal{L} indicate a smooth behavior. Although the optimum significance is generally in the range 0.6–0.7, a looser cut of $\mathcal{L} > 0.5$ is applied for all modes in order to reduce systematic uncertainties. This requirement removes (66–79)% of the continuum background samples while retaining (74–83)% of the signal samples.

For the $\bar{B}^0 \rightarrow D^0\omega$ mode the polarized nature of the ω allows additional discrimination against backgrounds to be achieved with an additional requirement of $|\cos\theta_{hel}| > 0.3$, where the helicity angle θ_{hel} is defined as the angle between the B flight direction in the ω rest frame and the vector perpendicular to the ω decay plane in the ω rest frame.

TABLE II: Efficiency correction factors for the modes $\bar{B}^0 \rightarrow D^{(*)0}h^0$; the correction factors for combined modes are averaged using PDG subdecay fractions.

Mode	D^0	$D^0(K\pi)$	$D^0(K\pi\pi^0)$	$D^0(K\pi\pi\pi)$
$D^0\pi^0$	0.94 ± 0.05	0.98 ± 0.05	0.90 ± 0.04	0.98 ± 0.06
$D^0\eta_{\gamma\gamma}$	0.99 ± 0.06	1.03 ± 0.06	0.95 ± 0.05	1.03 ± 0.07
$D^0\eta_{\pi^0\pi\pi}$	0.94 ± 0.06	0.98 ± 0.05	0.91 ± 0.05	0.98 ± 0.06
$D^0\eta_{\gamma\gamma+\pi^0\pi\pi}$	0.97 ± 0.06	–	–	–
$D^0\omega$	0.89 ± 0.06	0.92 ± 0.06	0.85 ± 0.06	0.92 ± 0.07
$D^{*0}\pi^0$	0.86 ± 0.09	0.90 ± 0.10	0.83 ± 0.09	0.90 ± 0.10
$D^{*0}\eta_{\gamma\gamma}$	0.91 ± 0.10	0.95 ± 0.10	0.88 ± 0.10	0.95 ± 0.11
$D^{*0}\omega$	0.83 ± 0.10	0.87 ± 0.10	0.80 ± 0.09	0.88 ± 0.11

TABLE III: Corrected efficiencies for the modes $\bar{B}^0 \rightarrow D^{(*)0}h^0$ excluding the subdecay branching fractions, for all D^0 modes combined and for the individual D^0 subdecay modes, as estimated for the ΔE fit samples.

Mode	D^0	$D^0(K\pi)$	$D^0(K\pi\pi^0)$	$D^0(K\pi\pi\pi)$
$D^0\pi^0$	0.075 ± 0.004	0.173 ± 0.008	0.042 ± 0.002	0.085 ± 0.005
$D^0\eta_{\gamma\gamma}$	0.061 ± 0.004	0.140 ± 0.008	0.036 ± 0.002	0.066 ± 0.004
$D^0\eta_{\pi^0\pi\pi}$	0.042 ± 0.003	0.092 ± 0.005	0.026 ± 0.002	0.046 ± 0.003
$D^0\eta_{\gamma\gamma+\pi^0\pi\pi}$	0.054 ± 0.003	0.122 ± 0.010	0.032 ± 0.003	0.058 ± 0.006
$D^0\omega$	0.025 ± 0.002	0.056 ± 0.004	0.015 ± 0.001	0.030 ± 0.002
$D^{*0}\pi^0$	0.036 ± 0.004	0.088 ± 0.009	0.019 ± 0.002	0.042 ± 0.005
$D^{*0}\eta_{\gamma\gamma}$	0.039 ± 0.004	0.093 ± 0.010	0.023 ± 0.003	0.042 ± 0.005
$D^{*0}\omega$	0.011 ± 0.001	0.026 ± 0.003	0.007 ± 0.001	0.011 ± 0.001

V. BACKGROUNDS FROM OTHER B DECAYS

Significant background contributions arise both from color-favored decays and from other color-suppressed decays (cross-feed) $\bar{B}^0 \rightarrow D^{*0}h^0$. Some backgrounds have the same final state as the signal while others mimic signal due to missing or extra particles.

Generic Monte Carlo [20] samples of $B\bar{B}$ and continuum $q\bar{q}$ are used to study the background contributions in the M_{bc} and ΔE distributions. The sample sizes correspond to approximately three times the expectations from the data sample analysed. The $B\bar{B}$ event sample excludes the color-suppressed modes under investigation. Signal mode samples for each of the decay chains considered are generated and reconstructed separately. They are used to estimate the cross-feed contributions between modes using the branching fractions measured here with an iterative procedure.

The dominant cross-feed contributions to the D^0h^0 decays are found to arise from the corresponding $D^{*0}h^0$ decays. These contributions peak at the same M_{bc} as the signal but are shifted to the lower side in ΔE . As can be seen from Figs. 3b and 4b, the cross-feed contribution is substantial in the region $-0.25 \text{ GeV} < \Delta E < -0.10 \text{ GeV}$ but quite small in the signal region. Cross-feed contributions to the $D^{*0}h^0$ decays are found to be small. In all cases, the fraction of cross-feed within the signal region is less than 10% of the observed yield.

For the $\bar{B}^0 \rightarrow D^{(*)0}\pi^0$ modes, the dominant background is from the color-allowed $B^- \rightarrow D^{(*)0}\rho^-$ decay. In the $\bar{B}^0 \rightarrow D^0\pi^0$ mode non-reconstructed soft π^0 from $D^{*0} \rightarrow D^0\pi^0$, photons from $D^{*0} \rightarrow D^0\gamma$ and π^- from $\rho^- \rightarrow \pi^-\pi^0$ produce the same final state as the signal. However, the missing particles cause a shift in ΔE with a broad peak centered at approximately $\Delta E = -0.2 \text{ GeV}$. In order to reduce contributions from this background, events that contain B candidates reconstructed as $B^- \rightarrow D^{(*)0}\rho^-$ within the signal region $5.27 \text{ GeV} < M_{bc} < 5.29 \text{ GeV}$ and $|\Delta E| < 0.1 \text{ GeV}$ are rejected. This requirement reduces the color-allowed contribution in the region $-0.25 \text{ GeV} < \Delta E < -0.10 \text{ GeV}$ by about 60%; it does little to reduce contributions in the signal region, but remains useful to facilitate background modelling. The M_{bc} distribution of these backgrounds is found to contribute at and slightly below the M_{bc} signal region; these are referred to as the “peaking background”.

For the \bar{B}^0 decays to $D^{(*)0}\eta$ and $D^{(*)0}\omega$ modes there are potential backgrounds arising from non-resonant $\bar{B}^0 \rightarrow D^{(*)0}\pi^+\pi^-\pi^0$ decays. Invariant mass, $M(\pi^+\pi^-\pi^0)$, distributions within the M_{bc} and ΔE signal regions indicate no significant contributions from these non-resonant decays. Ratios of data to Monte Carlo expectations in the invariant mass sidebands give values consistent with 1.0 with relative uncertainties in the range of 3–8 percent. As there are no indications of the presence of this background no systematic uncertainties from this source are assigned.

TABLE IV: Measured branching fractions ($\times 10^{-4}$) for the modes $\bar{B}^0 \rightarrow D^{(*)0}h^0$, using separate D^0 subdecay mode samples, as obtained from the ΔE fit.

Mode	$D^0(K\pi)$	$D^0(K\pi\pi^0)$	$D^0(K\pi\pi\pi)$
$D^0\pi^0$	$2.13 \pm 0.19 \pm 0.31$	$2.02 \pm 0.24 \pm 0.33$	$2.43 \pm 0.27 \pm 0.38$
$D^0\eta_{\gamma\gamma}$	$1.91 \pm 0.29 \pm 0.24$	$1.64 \pm 0.32 \pm 0.24$	$1.66 \pm 0.40 \pm 0.23$
$D^0\eta_{\pi^0\pi\pi}$	$1.52 \pm 0.44 \pm 0.26$	$1.51 \pm 0.46 \pm 0.28$	$2.18 \pm 0.60 \pm 0.39$
$D^0\omega$	$2.57 \pm 0.37 \pm 0.27$	$1.77 \pm 0.36 \pm 0.22$	$2.60 \pm 0.42 \pm 0.31$
$D^{*0}\pi^0$	$1.21 \pm 0.23 \pm 0.17$	$1.45 \pm 0.36 \pm 0.23$	$1.54 \pm 0.38 \pm 0.23$
$D^{*0}\eta_{\gamma\gamma}$	$1.43 \pm 0.42 \pm 0.25$	$0.79 \pm 0.44 \pm 0.15$	$2.09 \pm 0.57 \pm 0.38$
$D^{*0}\omega$	$2.66 \pm 0.64 \pm 0.38$	$1.90 \pm 0.62 \pm 0.31$	$2.12 \pm 0.76 \pm 0.38$

VI. DATA MODELLING AND SIGNAL EXTRACTION

Independent unbinned extended maximum likelihood fits to the ΔE and M_{bc} distributions are performed to obtain the signal yields. The yields from the ΔE fits are used to extract the branching fractions, while the yields from the M_{bc} fits are used to cross-check the results. The principal parameters of the fits are the normalization factors of the components used to model the observed distributions. The ΔE fit is performed in the range $-0.25 \text{ GeV} < \Delta E < 0.25 \text{ GeV}$ using the M_{bc} signal sample while the M_{bc} fit is performed in the range $M_{bc} > 5.2 \text{ GeV}/c^2$ using the mode-dependent ΔE signal samples. In most cases the shapes of the signal and background component distributions in M_{bc} and ΔE are obtained from fits to MC samples.

The signal models used are the same for all modes, with the M_{bc} signals modeled with a Gaussian function and the ΔE signals modeled with an empirical formula known as the Crystal Ball (CB) line shape [21], that accounts for the asymmetric calorimeter energy response. The CB function is added to a Gaussian function in ΔE with the same

mean. Fits of the ΔE distributions to signal Monte Carlo for each final state are used to obtain the signal shape parameters.

The cross-feed contributions in M_{bc} and ΔE are studied using a combination of signal Monte Carlo samples from all other color suppressed modes, weighted according to the branching fractions obtained here. Smoothed histograms obtained from this combined sample are used as estimates of the cross-feed contributions. In the M_{bc} case the ΔE signal region requirement results in very small cross-feed contributions, which are fixed at the Monte Carlo expectation. For ΔE there are considerable contributions in the region $-0.25 \text{ GeV} < \Delta E < -0.10 \text{ GeV}$. The normalization of this component is allowed to float in the fit for the $D^0 h^0$ modes; for the $D^{*0} h^0$ modes the cross-feed expectations are small and are fixed at the Monte Carlo expectation.

Continuum-like backgrounds in the M_{bc} fits are modeled by an empirical threshold function known as the ARGUS function [22]. The small peaking background contributions are modeled by a Gaussian of mean and width and normalization obtained by a fit to the $B\bar{B}$ background Monte Carlo M_{bc} distribution, using an ARGUS function plus a Gaussian. A systematic uncertainty of 50% is assigned to the determination of this small background distribution. This treatment allows the vast majority of the background to be simply modeled with the ARGUS shape, leaving a small but less well-known peaking background component that represents the deviation from the ARGUS shape.

In fits to data M_{bc} distributions, the ARGUS background function parameters are fixed to the values obtained from fits to combined Monte Carlo $B\bar{B}$ and continuum background samples. The signal parameters are free, as are the normalizations of signal and background. The small peaking background and cross-feed contributions are fixed at their expected values.

The ΔE background distributions in the $\bar{B}^0 \rightarrow D^0 \eta$ and $\bar{B}^0 \rightarrow D^0 \omega$ are modeled using smoothed histograms obtained from a combined continuum and generic $B\bar{B}$ Monte Carlo sample. For the $\bar{B}^0 \rightarrow D^{(*)0} \pi^0$ modes, the shapes of the ΔE distribution arising from $B\bar{B}$ and continuum background are very different (see Fig. 2) necessitating separate modelling. The continuum shape is modeled with a first-order polynomial with slope obtained from fits to the continuum Monte Carlo sample. The shape of the $B\bar{B}$ background is modeled with a Gaussian function plus a second-order polynomial, with parameters determined from a fit to the generic $B\bar{B}$ Monte Carlo sample. In fits to data, the large peak in the region $-0.25 \text{ GeV} < \Delta E < -0.10 \text{ GeV}$ that arises principally from the color-allowed $B^- \rightarrow D^{(*)0} \rho^-$ decays is found to be broader than the Monte Carlo expectation; thus all parameters of this color-allowed Gaussian are allowed to float in the fit. The normalizations of the contributions from the remainder of the $B\bar{B}$ background, the continuum and the signal are also floated in the fit, with the small cross-feed contribution fixed as discussed above.

The results of the M_{bc} and ΔE fits for each of the $D^{(*)0} h^0$ modes with the three D^0 subdecay modes combined are presented in Figs. 2, 3 and 4. The $D^{(*)0} h^0$ mode results are obtained by a simultaneous fit to the three submodes, where the signal yields in each submode are constrained by the ratios of the products of efficiency and secondary branching fraction.

TABLE V: Systematic uncertainties of the measured branching fractions for $\bar{B}^0 \rightarrow D^{(*)0} h^0$, for the combined D^0 submode samples, as estimated for the ΔE fit results.

Category	$D^0 \pi^0$	$D^0 \eta_{\gamma\gamma}$	$D^0 \eta_{\pi^0 \pi\pi}$	$D^0 \eta_{\gamma\gamma + \pi^0 \pi\pi}$	$D^0 \omega$	$D^{*0} \pi^0$	$D^{*0} \eta_{\gamma\gamma}$	$D^{*0} \omega$
Tracking efficiency	2.6	2.6	2.6	2.6	2.6	2.6	2.6	2.6
h^0 efficiency	2.7	4.0	4.0	4.0	5.4	2.7	4.0	5.4
Kaon efficiency	1.0	1.0	1.0	1.0	1.0	1.0	1.0	1.0
Extra π^0 efficiency	0.8	0.8	0.8	0.8	0.8	0.8	0.8	0.8
Likelihood ratio efficiency	3.0	3.0	3.0	3.0	3.0	3.0	3.0	3.0
MC statistics	2.1	2.1	2.6	2.3	3.0	3.3	2.6	5.3
Slow π^0 (from D^{*0}), efficiency	0.0	0.0	0.0	0.0	0.0	9.5	9.5	9.5
Crossfeed	1.1	1.1	1.1	1.1	1.6	0.4	1.1	0.9
Modelling $\pm 1\sigma$ variations	13.6	11.1	16.0	8.3	7.4	12.9	12.3	6.4
Subdecay Branching Fractions	5.2	5.2	5.5	5.3	5.2	7.1	7.1	7.1
Number of $B\bar{B}$ events	0.7	0.7	0.7	0.7	0.7	0.7	0.7	0.7
Longitudinal polarization fraction	-	-	-	-	-	-	-	7.1
Total (%)	15.6	13.8	18.1	11.7	11.9	18.5	18.3	17.6

VII. BRANCHING FRACTION RESULTS

The yields obtained from the M_{bc} and ΔE fits are consistent; the difference is typically within 50% of the statistical uncertainty. The results from the ΔE fits are found to have a slightly smaller total uncertainty in most cases and are used for the final result. The yields for the $D^{(*)0}h^0$ modes (with the three D^0 subdecay samples combined) obtained from the one dimensional ΔE fits are presented in Table I. The statistical significances of the signals for each of the combined subdecay samples are greater than 6σ . The combined $\eta \rightarrow \gamma\gamma$ and $\eta \rightarrow \pi^+\pi^-\pi^0$ yields are obtained from a combined fit to the individual η samples, rather than from a summation of the individual sample yields. The agreement between these approaches is apparent from the Table. For the D^0h^0 modes, backgrounds arising from cross-feed contributions in the signal region can be seen to contribute substantially less than the extent of the statistical uncertainty on the signal yield.

The yields obtained are interpreted as branching fractions using the number of $B\bar{B}$ events, the product of subdecay fractions [23] corresponding to the decay of D^0h^0 or $D^{*0}h^0$ into the observed final states, and the efficiency. The efficiency for each mode is first obtained from signal Monte Carlo samples and then corrected to account for differences between data and MC expectations.

The total efficiency corrections for each final state are obtained from the product of the relevant efficiency correction factors. The values for all final states of the $D^{(*)0}h^0$ modes are presented in Table II and the efficiencies are presented in Table III.

For the $D^{*0}h^0$ modes, the correction to the reconstruction efficiency of the soft pion produced in the process $D^{*0} \rightarrow D^0\pi^0$ is estimated to be 0.920 ± 0.087 ; this dominates the correction value and uncertainty for these modes. This soft pion efficiency correction is estimated by comparing the yields of D^{*+} from the processes $D^{*+} \rightarrow D^0\pi^+$ and $D^{*+} \rightarrow D^+\pi^0$, using the subdecay modes $D^0 \rightarrow K^-\pi^+$, $D^0 \rightarrow K^-\pi^+\pi^+\pi^-$ and $D^+ \rightarrow K^-\pi^+\pi^+$. The final states differ by a single π^0 or π^+ , allowing the ratio of yields of $D^{*+} \rightarrow D^0\pi^+$ and $D^{*+} \rightarrow D^+\pi^0$ to be used to estimate the ratio of efficiencies between soft π^+ and π^0 . Forming a double ratio of data over Monte Carlo and using separate estimates for the soft π^+ efficiency correction provides the soft π^0 efficiency correction factor. The uncertainties on this factor are dominated by the uncertainties on the subdecay branching fractions. Reconstruction efficiencies for more energetic π^0 's are obtained from comparisons of $\eta \rightarrow \pi^0\pi^0\pi^0$ to $\eta \rightarrow \gamma\gamma$ and to $\eta \rightarrow \pi^+\pi^-\pi^0$, for data and Monte Carlo.

TABLE VI: Measured branching fractions ($\times 10^{-4}$) for the modes $\bar{B}^0 \rightarrow D^{(*)0}h^0$, obtained from simultaneous fits to the three D^0 subdecay mode samples as obtained from the ΔE fit.

Mode	Branching fraction ($\times 10^{-4}$)
$D^0\pi^0$	$2.25 \pm 0.14 \pm 0.35$
$D^0\eta\gamma\gamma$	$1.77 \pm 0.20 \pm 0.24$
$D^0\eta\pi^0\pi\pi$	$1.78 \pm 0.30 \pm 0.32$
$D^0\eta\gamma\gamma+\pi^0\pi\pi$	$1.77 \pm 0.16 \pm 0.21$
$D^0\omega$	$2.37 \pm 0.23 \pm 0.28$
$D^{*0}\pi^0$	$1.39 \pm 0.18 \pm 0.26$
$D^{*0}\eta\gamma\gamma$	$1.40 \pm 0.28 \pm 0.26$
$D^{*0}\omega$	$2.29 \pm 0.39 \pm 0.40$

TABLE VII: Ratios of branching fractions, $\frac{\bar{B}^0 \rightarrow D^0h^0}{\bar{B}^0 \rightarrow D^{*0}h^0}$, with statistical and systematic uncertainties.

Modes	Ratio of branching fractions
$\frac{D^0\pi^0}{D^{*0}\pi^0}$	$1.62 \pm 0.23 \pm 0.35$
$\frac{D^0\eta\gamma\gamma}{D^{*0}\eta\gamma\gamma}$	$1.27 \pm 0.29 \pm 0.25$
$\frac{D^0\omega}{D^{*0}\omega}$	$1.04 \pm 0.20 \pm 0.17$

The branching fraction results obtained from the ΔE fit yields for the $D^{(*)0}h^0$ modes with the D^0 submodes combined are provided in Table VI. Results from the individual submodes are shown in Table IV. These results are also graphically presented in Fig. 5, where the BaBar [5] results from a one dimensional fit to M_{bc} distributions are also included for comparison. Table VII presents the measured ratios of branching fractions, which benefit from a partial cancellation of systematic uncertainties.

TABLE VIII: Dependency coefficients expressing the relative changes to the branching fractions provided in Table VI due to relative changes to the D^0 branching fractions. The uncertainties presented are propagated from the uncertainties on the efficiencies only.

Mode	$D^0(K\pi)$	$D^0(K\pi\pi^0)$	$D^0(K\pi\pi\pi)$
$D^0\pi^0$	0.352 ± 0.034	0.311 ± 0.030	0.337 ± 0.032
$D^0\eta\gamma\gamma$	0.350 ± 0.038	0.329 ± 0.036	0.321 ± 0.035
$D^0\eta_{\pi^0\pi\pi}$	0.335 ± 0.037	0.339 ± 0.038	0.327 ± 0.036
$D^0\eta_{\gamma\gamma+\pi^0\pi\pi}$	0.344 ± 0.038	0.333 ± 0.036	0.323 ± 0.035
$D^0\omega$	0.334 ± 0.044	0.318 ± 0.042	0.347 ± 0.045
$D^{*0}\pi^0$	0.368 ± 0.072	0.285 ± 0.056	0.346 ± 0.068
$D^{*0}\eta\gamma\gamma$	0.362 ± 0.072	0.319 ± 0.064	0.319 ± 0.064
$D^{*0}\omega$	0.356 ± 0.079	0.341 ± 0.076	0.303 ± 0.067

Table VIII provides the fractional dependence of the B^0 branching fractions listed in Table VI upon the D^0 branching fractions. These allow corrections to the measurements to be made to account for improved determinations of the branching fractions [23] : $\mathcal{B}(D^0 \rightarrow K^-\pi^+) = (3.89 \pm 0.09)\%$, $\mathcal{B}(D^0 \rightarrow K^-\pi^+\pi^+) = (13.9 \pm 0.9)\%$ and $\mathcal{B}(D^0 \rightarrow K^-\pi^+\pi^+\pi^-) = (7.49 \pm 0.31)\%$. The coefficients are obtained from the subdecay branching fractions and the efficiencies for each subdecay. The fractional change to the branching fractions can be obtained from the product of the relative change of the subdecay branching fraction and the corresponding negated coefficient.

VIII. SYSTEMATIC UNCERTAINTIES

Systematic uncertainties estimated for the D^0h^0 and $D^{*0}h^0$ modes for the combined D^0 submode samples are provided in Table V. The systematic uncertainties are obtained by averaging those for the individual final states using the PDG D^0 subdecay fractions. The “Tracking efficiency” category accounts for charged products of $D^{(*)0}$ only, estimated using an uncertainty of 1% per charged track. The “ h^0 efficiency” category corresponds to efficiency uncertainties for π^0 , η and ω . These uncertainties are obtained from the uncertainty on the efficiency corrections which is estimated from comparisons of ratios of various processes between data and Monte Carlo samples, as outlined in the previous section. The “Extra π^0 ” category corresponds to the π^0 from the $D^0 \rightarrow K^-\pi^+\pi^0$ process.

The cross-feed uncertainty is estimated as 25% of the contribution from this source in the signal regions. Uncertainties arising from the background and signal modelling used are estimated from the changes in the yields as a result of $\pm 1\sigma$ variations on the model parameters.

The “Longitudinal polarization fraction” uncertainty is relevant only for the vector-vector final state $D^{*0}\omega$. Although the analysis does not directly use angular information in these modes, the polarization can effect the orientation and hence momentum of the slow π^0 from the D^{*0} resulting in changes to the total efficiency. Monte Carlo signal samples with various longitudinal polarization fractions (f_L) are used to estimate the size of the effect. The results are quoted assuming $f_L = 0.5 \pm 0.5$; the variation in the efficiency over the full range of possible values is used to estimate the systematic uncertainty.

The dominant contributions arise from the background and signal modelling, slow π^0 efficiency for D^{*0} modes, and the subdecay branching fractions. The total uncertainty is obtained by summing the individual uncertainties in quadrature.

IX. CONCLUSION

Improved measurements of the branching fractions of the color-suppressed decays $\bar{B}^0 \rightarrow D^0\pi^0$, $D^0\eta$, $D^0\omega$, $D^{*0}\pi^0$, $D^{*0}\eta$ and $D^{*0}\omega$ are presented. The results are consistent with the previous Belle measurements but with considerably improved precision due to the sevenfold increase in statistics. The individual results are consistent within two standard deviations with the BaBar measurements [5]; however it is notable that all the measurements are lower than those of BaBar.

The measured values fall in the range $(1.4\text{--}2.4) \times 10^{-4}$, which is significantly higher than theoretical predictions based on naive factorization. This discrepancy indicates that either final state rescattering is significant, or else the assumption that the second Wilson coefficient a_2 is real and process-independent is invalid [9, 10].

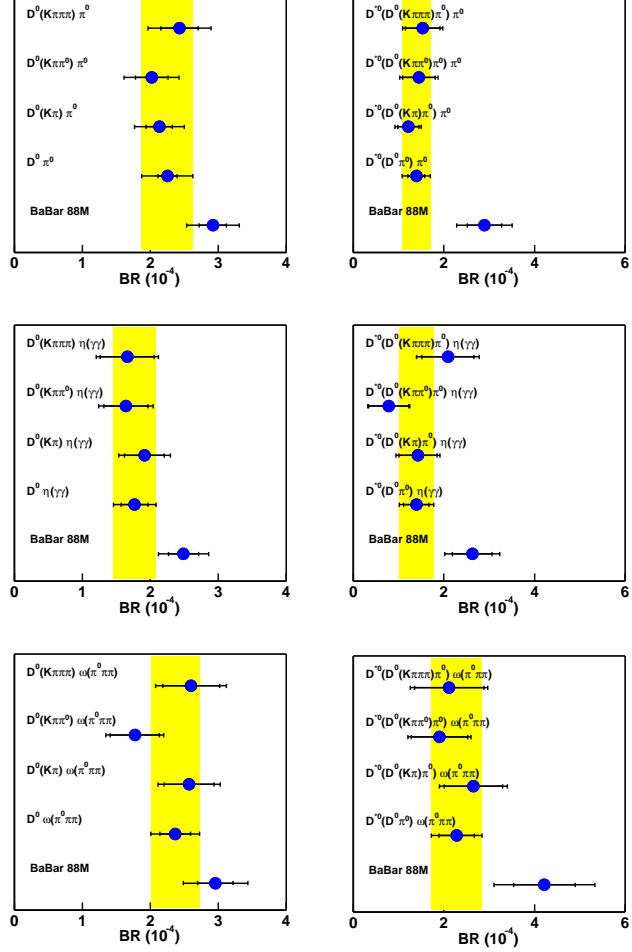


FIG. 5: Comparison of the measured branching fractions ($\times 10^{-4}$) of the modes $\bar{B}^0 \rightarrow D^{(*)0} h^0$, for each of the three D^0 subdecay modes and for the combined mode samples, as obtained from the ΔE fit, with the M_{bc} signal region requirement applied. The shaded band indicates the combined submode result. The BaBar results [5] from M_{bc} fits are also shown.

Acknowledgments

We thank the KEKB group for the excellent operation of the accelerator, the KEK cryogenics group for the efficient operation of the solenoid, and the KEK computer group and the National Institute of Informatics for valuable computing and Super-SINET network support. We acknowledge support from the Ministry of Education, Culture, Sports, Science, and Technology of Japan and the Japan Society for the Promotion of Science; the Australian Research Council and the Australian Department of Education, Science and Training; the National Science Foundation of China and the Knowledge Innovation Program of Chinese Academy of Sciences under contract No. 10575109 and IHEP-U-503; the Department of Science and Technology of India; the BK21 program of the Ministry of Education of Korea, and the CHEP SRC program and Basic Research program (grant No. R01-2005-000-10089-0) of the Korea Science and Engineering Foundation; the Polish State Committee for Scientific Research under contract No. 2P03B 01324; the Ministry of Science and Technology of the Russian Federation; the Slovenian Research Agency; the Swiss National Science Foundation; the National Science Council and the Ministry of Education of Taiwan; and the U.S. Department

of Energy.

[1] Throughout this paper, the inclusion of the charge conjugate mode decay is implied unless otherwise stated.

[2] Belle Collaboration, A. Satpathy *et al.*, Phys. Lett. B **553**, 159 (2003).

[3] Belle Collaboration, K. Abe *et al.*, Phys. Rev. Lett. **88**, 052002 (2002).

[4] CLEO Collaboration, T.E. Coan *et al.*, Phys. Rev. Lett. **88**, 062001 (2002).

[5] BaBar Collaboration, B. Aubert *et al.*, Phys. Rev. D **69**, 032004 (2004).

[6] Belle Collaboration, J. Schümann *et al.*, Phys. Rev. D **72**, 011103(R) (2005).

[7] M. Beneke, G. Buchalla, M. Neubert, and C.T. Sachrajda, Nucl. Phys. B **591**, 313 (2000).

[8] M. Neubert and B. Stech, in *Heavy Flavours II*, eds. A.J. Buras and M. Lindner (World Scientific, Singapore, 1998), p. 294 [hep-ph/9705292].

[9] M. Neubert and A.A. Petrov, Phys. Lett. B **519**, 50 (2001).

[10] C-K. Chua, W-S. Hou, and K-C. Yang, Phys. Rev. D **65**, 096007 (2002).

[11] J.L. Rosner, Phys. Rev. D **60**, 074029 (1999).

[12] A. Deandrea and A.D. Polosa, Eur. Phys. Jour. C **22**, 677 (2002).

[13] C-W. Chiang and J.L. Rosner, Phys. Rev. D **67**, 074013 (2003).

[14] S. Mantry, D. Pirjol, and I.W. Stewart, Phys. Rev. D **68**, 114009 (2003); C.W. Bauer, D. Pirjol, and I.W. Stewart, Phys. Rev. Lett. **87**, 201806 (2001); C.W. Bauer, B. Grinstein, D. Pirjol, and I.W. Stewart, Phys. Rev. D **67**, 014010 (2003).

[15] Y-Y. Keum *et al.*, Phys. Rev. D **69**, 094018 (2004); C.D. Lu, Phys. Rev. D **68**, 097502 (2003).

[16] S. Kurokawa and E. Kikutani, Nucl. Instr. and. Meth. A **499**, 1 (2003), and other papers included in this volume.

[17] Belle Collaboration, P. Krokovny *et al.*, Phys. Rev. Lett. **97**, 081801 (2006).

[18] Belle Collaboration, A. Abashian *et al.*, Nucl. Instr. and Meth. A **479**, 117 (2002).

[19] The Fox-Wolfram moments were introduced in G. C. Fox and S. Wolfram, Phys. Rev. Lett. **41**, 1581 (1978). The Fisher discriminant used by Belle, based on modified Fox-Wolfram moments (SFW), is described in Belle Collaboration, K. Abe *et al.*, Phys. Rev. Lett. **87**, 101801 (2001) and Belle Collaboration, K. Abe *et al.*, Phys. Lett. B **511**, 151 (2001).

[20] Events are generated with the CLEO QQ generator (see <http://www.lns.cornell.edu/public/CLEO/soft/QQ>); the detector response is simulated with GEANT, R. Brun *et al.*, GEANT 3.21, CERN Report DD/EE/84-1, 1984.

[21] J. E. Gaiser *et al.*, Phys. Rev. D **34**, 711 (1986).

[22] ARGUS Collaboration, H. Albrecht *et al.*, Phys. Lett. B **229**, 304 (1989).

[23] S. Eidelman *et al.*, Phys. Lett. B **592**, 1 (2004).